

# CleanPose: Category-Level Object Pose Estimation via Causal Learning and Knowledge Distillation

Xiao Lin, Yun Peng, Liuyi Wang, Xianyou Zhong, Minghao Zhu, Jingwei Yang, Chengju Liu, Qijun Chen\*  
 School of Electronic and Information Engineering, Tongji University, Shanghai, China  
 {linx\_xx, pengyun, wly, zhongxianyou, zmhh\_h, jw\_yang, liuchengju, qjchen}@tongji.edu.cn

## Abstract

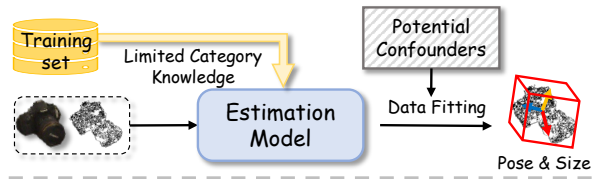
Category-level object pose estimation aims to recover the rotation, translation and size of unseen instances within predefined categories. In this task, deep neural network-based methods have demonstrated remarkable performance. However, previous studies show they suffer from spurious correlations raised by “unclean” confounders in models, hindering their performance on novel instances with significant variations. To address this issue, we propose **CleanPose**, a novel approach integrating causal learning and knowledge distillation to enhance category-level pose estimation. To mitigate the negative effect of unobserved confounders, we develop a causal inference module based on front-door adjustment, which promotes unbiased estimation by reducing potential spurious correlations. Additionally, to further improve generalization ability, we devise a residual-based knowledge distillation method that has proven effective in providing comprehensive category information guidance. Extensive experiments across multiple benchmarks (REAL275, CAMERA25 and HouseCat6D) highlight the superiority of proposed CleanPose over state-of-the-art methods. Code will be released.

## 1. Introduction

Category-level object pose estimation (COPE) aims to predict the 3D rotation, 3D translation and 3D metric size, for arbitrary objects within predefined categories. This task, unlike instance-level pose estimation [9, 12, 19, 24, 47, 64], does not require high-quality CAD models, making it feasible to perceive a broader range of novel objects instead of a single instance. In recent years, this task has garnered significant attention due to its essential role in various practical applications, including augmented reality [34], autonomous driving [3] and robotic manipulation [44], *etc.*

The core challenge of COPE lies in the complicated and diverse intra-category variations. To obtain robust cate-

(a) Existing approaches affected by confounders



(b) Our proposed causal learning pipeline

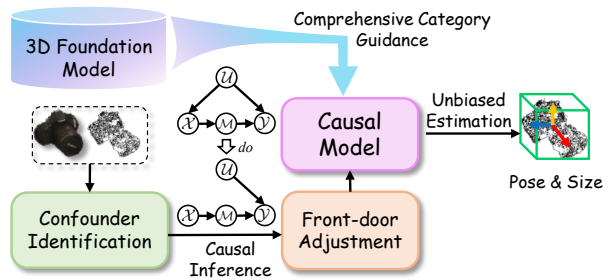


Figure 1. Comparison of (a) existing pose estimation approaches with (b) the proposed causal learning pipeline. The front-door adjustment is used to mitigate the negative effect from confounders. We also leverage rich 3D semantic knowledge to provide comprehensive category guidance.

gory features and achieve accurate pose prediction, previous methods [4, 5, 22, 23, 25, 26, 29, 62, 63] largely rely on deep neural networks (DNNs) due to their significant learning and modeling capabilities, offering impressive progress. Although DNNs have demonstrated extraordinary performance in COPE, recent studies [16, 49] reveal that they may focus on spurious correlations to benefit predictions, as their optimization objective is to learn statistical distribution only. These illogical correlations in models are typically raised by the underlying *confounders* [38] behind the task, *e.g.*, dataset biases [17, 60]. Here, confounders are variables that influence both inputs and outcomes. DNN-based pose estimation models are sensitive to the confounders during data fitting, as shown in Fig. 1(a). For instance, the COPE models may overfit to specific objects’ appearance and poses due to the lack of data variety in dataset, damaging the generalization to novel instances

\*Corresponding author.

Another important aspect of COPE neglected by previous works is the comprehensive category-specific guidance. Most of them [4, 5, 23, 25, 28] solely derive category information from a limited instances per category in training set, which may also capture only limited category diversity. One way to tackle above two issues is to create broader and more diverse datasets [7, 17, 50, 60], though valuable, achieving a perfectly balanced dataset free of bias remains nearly impossible. Additionally, the dataset’s scale is still significantly constrained by the cost of 3D data annotation [61].

To better address the dilemma, we direct our attention to the human observation mechanism. In fact, the reason why humans can effectively handle variations among intra-category objects is that we learn inherent causality beyond biased observation, achieving excellent analogical association capability. Motivated by this finding, for the first time, we propose to incorporate the causal inference [36, 37] into the formulation of COPE. In this way, we can investigate the causal relation among variables and equip COPE models with similar cognitive abilities that human have. Technically, it is non-trivial to incorporate the causal learning in COPE applications because of the following challenges: (i) The unique modality of 3D data makes it impractical to directly apply existing causal modeling techniques [15]. (ii) Subsequently, the confounders in pose estimation task are inherently unobserved and elusive, which further increases the challenge of identifying these confounders and mitigating their negative impacts. (iii) Moreover, enhancing the model’s category generalization capability can not be overlooked. How to improve the generalization while simultaneously deconfounding needs to be carefully considered.

To this end, we present **CleanPose**, a concise yet effective framework with causal learning [36] and knowledge distillation to enhance the category-level pose estimation, as shown in Fig. 1(b). Faced with the challenge that hidden confounders are elusive or even unobserved in our task, we propose to develop a causal inference approach based on *front-door adjustment*, which can effectively approximate the predicted expectations by potential confounders. Moreover, to create suitable dictionary for representing confounders, we devise and maintain the dictionary as a dynamic queue, similar with MoCo [11], to efficiently update training samples. To further address the weakness in category information guidance, we design a residual-based feature knowledge distillation layer to transfer abundant point cloud category information of powerful 3D foundation model, ULIP-2 [53], to guide the category feature learning within the model. As demonstrated by extensive experiments, our findings reveal the impact of integrating causal learning to deconfound biases, and providing comprehensive category information on COPE, enhancing the model’s robustness and generalization.

To summarize, our main contributions are as follows:

- We propose CleanPose, a pioneering solution to mitigate the confounding effect in category-level pose estimation via causal learning. Taking inspiration from human observation mechanism, we propose to identify the causal effect to achieve unbiased estimation, recovering correct pose of novel instances within category.
- We develop a residual category knowledge distillation approach to transfer rich 3D category knowledge from 3D foundation models into category-level networks, enhancing the intra-category generalization.
- Our proposed CleanPose achieves state-of-the-art performance on three mainstream challenge benchmarks (REAL275 [48], CAMERA25 [48] and House-Cat6D [17]). For instance, the accuracy attains **61.5%** on rigorous metric  $5^{\circ}2\text{ cm}$  of REAL275 dataset, surpassing the current best method with a large margin by 4.5%.

## 2. Related Works

**Category-level Object Pose Estimation.** The objective of this task encompasses predicting the 9DoF pose for unseen objects within predefined categories. To address this challenging task, pioneer method NOCS [48] suggests mapping input shape to a normalized canonical space and recovering the pose via Umeyama algorithm [45]. SPD [43] proposes a method for deriving and utilizing the shape prior for each category. This crucial insight inspires many subsequent prior-based works [6, 20], which further improve the use of shape priors, continuously improving the pose estimation performance. More recently, prior-free methods [4, 5, 23, 25, 62] have achieved impressive performance. VI-Net [23] separates rotation into viewpoint and in-plane rotations, while SecondPose [4] propose to extract hierarchical panel-based geometric features for point cloud. AG-Pose [25] achieves current state-of-the-art performance by explicitly extract local and global geometric keypoint information of different instances. However, above methods have not fully considered that DNNs lack the ability to perform causal inference, which may leads the models to learn spurious correlations. In addition, most of them either explicitly or implicitly learn category information from training set, which results in poor generalization ability to unseen instances within the categories.

**Knowledge Distillation.** Knowledge distillation [13] is a technique that transfers knowledge from a teacher model to a student model. Transferring the knowledge of foundation models for downstream tasks has been proven to be effective [8, 14, 66]. ViLD [8] distill knowledge from CLIP [41] to achieve open-vocabulary object detection, while some methods [14, 66] utilize the generalizability of VLMs to address the video recognition task. The most related method to our work is CLIPose [26]. It aligns the representations of the image, point cloud, and text modalities through multi-modal contrastive learning. However, such semantic la-

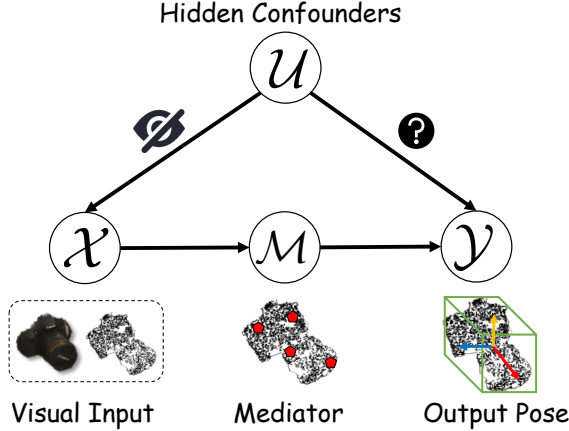


Figure 2. Illustration of the structural causal model of COPE.

bels cannot effectively guide the perception of point cloud structural information. Unlike CLIPose, our method distills knowledge directly from the point cloud encoder of 3D foundation models via a residual MLP layer, providing more comprehensive guidance for category learning.

**Causal Inference.** Causality [36] is an emerging technique referring to the modeling the relationships between factors in a task from a human perspective. Recent methods have incorporated causal inference to improve the performance of DNNs in computer vision domains, *e.g.*, object detection [51, 57], image captioning [27, 54] and vision-language task [49, 55, 59]. Though valuable, these methods can flexibly identify confounders due to natural prompts in data, *e.g.*, the keywords in instructions [49] and salient regions in an image [51], which are inapplicable for point cloud data.

In 3D domain, several works have focused on enhancing the robustness of point cloud classification [15] or 3D reconstruction [30] with causal inference. However, it is non-trivial to adapt these approaches to pose estimation due to the inherent differences in human modeling among these tasks. In this work, we propose a specific causal learning approach based on front-door adjustment for category-level pose estimation for the first time.

### 3. Preliminary

#### 3.1. Task Formulation

Given an RGB-D image containing objects from a predefined set of categories, off-the-shelf segmentation models such as MaskRCNN [10] are employed to obtain masks and category labels for each object in the images. Then, the segmentation masks can be utilized to get the cropped RGB image  $\mathcal{I}_{obj} \in \mathbb{R}^{H \times W \times 3}$  and the point cloud  $\mathcal{P}_{obj} \in \mathbb{R}^{N \times 3}$ , where  $N$  is the number of points and  $\mathcal{P}_{obj}$  is acquired by back-projecting the cropped depth image with camera intrinsics followed by a downsampling process. With the input  $\mathcal{I}_{obj}$  and  $\mathcal{P}_{obj}$ , the objective of COPE [48] is to recover

the 9DoF poses, including the 3D rotation  $\mathcal{R} \in SO(3)$ , the 3D translation  $t \in \mathbb{R}^3$  and 3D metric size  $s \in \mathbb{R}^3$ .

#### 3.2. The Causal Modeling of CleanPose

To quantify the underlying logic behind human observation, we construct a structural causal model [36, 37] capturing the relationships among the key variables in COPE: visual input  $\mathcal{X}$ , output pose  $\mathcal{Y}$ , mediator  $\mathcal{M}$  and hidden confounders  $\mathcal{U}$ . We illustrate the causal model in Fig. 2, where each direct link denotes a causal relationship between two nodes.

- $\mathcal{X} \rightarrow \mathcal{M} \rightarrow \mathcal{Y}$  (*Front-door path*): Typically, humans first recognize the structural information of an object, *i.e.*, keypoints [25, 62], and then determine the object’s pose based on the similar poses of other objects within this category. This process involves identifying keypoints of the object and their relative positions, and leveraging this information to perform pose estimation. We use mediator  $\mathcal{M}$  to represent such structural information and describe such process via the causal path  $\mathcal{X} \rightarrow \mathcal{M} \rightarrow \mathcal{Y}$ , which is also referred to as the *front-door path*.
- $\mathcal{X} \leftarrow \mathcal{U} \rightarrow \mathcal{Y}$  (*Hidden confounders*): The confounders are extraneous variables that influence both inputs and outputs, *e.g.*, dataset biases [17, 60] or category specific attributes [43].  $\mathcal{U} \rightarrow \mathcal{X}$  exists because the input data is inevitably affected by the limited resources in real world and sampling noises from sensors when collection and simulation. Moreover,  $\mathcal{U} \rightarrow \mathcal{Y}$  emerges because collected scenes, annotation bias, or the variety of pose also affect the probability of pose distributions. Traditional DNNs-based COPE methods tend to model the statistical correlations  $P(\mathcal{Y}|\mathcal{X})$ , given the optimization goal of maximizing the pose accuracy [63]. With the lack of modeling of hidden confounders, no matter how large the amount of training data is, the model can not identify the true causal effect from  $\mathcal{X}$  to  $\mathcal{Y}$ .

## 4. Methodology

### 4.1. Feature Extractor

Following [25], we utilize the PointNet++ [40] to extract point feature  $\mathcal{F}_P \in \mathbb{R}^{N \times C_1}$  of input point cloud  $\mathcal{P}_{obj}$ . As for the RGB image  $\mathcal{I}_{obj}$ , we adopt DINOv2 [35] as our image feature extractor, which has been proven to extract abundant semantic-aware information from RGB images [39]. We select those pixel features corresponding to  $\mathcal{P}_{obj}$  and utilize linear interpolation to propagate the original DINOv2 features into the final RGB features  $\mathcal{F}_I \in \mathbb{R}^{N \times C_2}$ . Eventually, we concatenate  $\mathcal{F}_P$  and  $\mathcal{F}_I$  to form  $\mathcal{F}_{obj} \in \mathbb{R}^{N \times C}$  as the input for the subsequent networks.

### 4.2. Causal Inference of CleanPose

**The Adjustment Formulation.** To avoid making the pose estimation process overfit to specific hidden confounders,

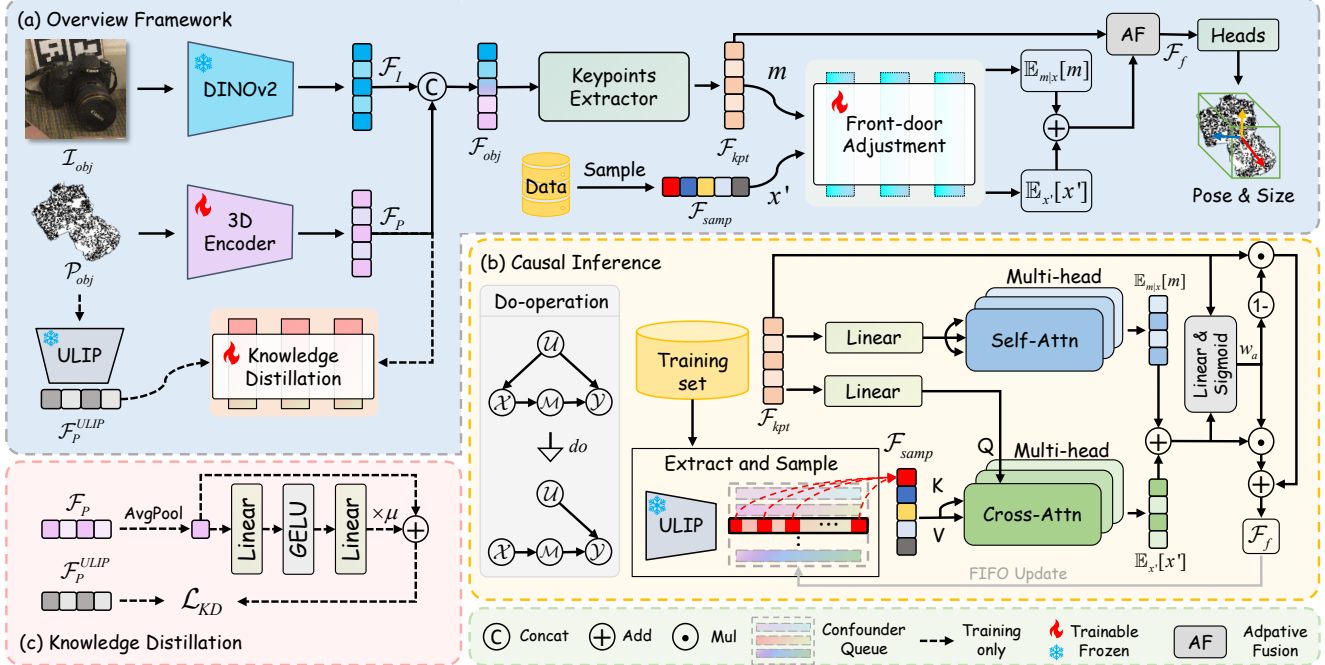


Figure 3. (a) Framework of CleanPose. (b) Causal inference based on front-door adjustment is employed for mitigating potential spurious correlations, promoting unbiased pose estimation. Moreover, the proposed (c) residual-based knowledge distillation module can efficiently provide comprehensive category-specific guidance.

we propose to perform robust modeling according to the causal graph and exploit *intervention* [36] to alleviate the negative effects raised by confounders. Specifically, we employ *do*-operation [37], which provides scientifically sound methods for determining causal effects, as shown in Fig. 3(b). The specific process of intervention via *do*-operation is as follow. Based on Bayes’s theorem, the typical observational likelihood is as:

$$P(\mathcal{Y}|\mathcal{X}) = \sum_u P(\mathcal{Y}|\mathcal{X}, u)P(u|\mathcal{X}), \quad (1)$$

where  $P(u|\mathcal{X})$  would bring biased weights. Then we perform the *do*-operation on inputs  $\mathcal{X}$ , which amounts to removing all edges directed into that variable in the graph model, *i.e.*, from hidden confounders  $\mathcal{U}$ . According to the invariance and independence rules [37], we have:

$$P(\mathcal{Y}|do(\mathcal{X})) = \sum_u P(\mathcal{Y}|do(\mathcal{X}), u)P(u|do(\mathcal{X})) \quad (2)$$

$$= \sum_u P(\mathcal{Y}|\mathcal{X}, u)P(u). \quad (3)$$

In this way, the intervention is realized by blocking the causal path  $\mathcal{U} \rightarrow \mathcal{X}$ . The Eq. (3) is also known as the *adjustment formulation* [36].

**Front-door Adjustment Causal Learning.** In the previous section, we have clarified meaning of the *front-door path*  $\mathcal{X} \rightarrow \mathcal{M} \rightarrow \mathcal{Y}$ . In COPE task, the DNNs-based models  $P(\mathcal{Y}|\mathcal{X}) = \sum_m P(\mathcal{Y}|m)P(m|\mathcal{X})$  will choose the suitable knowledge  $\mathcal{M}$  from input  $\mathcal{X}$  for pose estimation results  $\mathcal{Y}$ .

Due to the presence of the mediators  $\mathcal{M}$ , applying adjustment Eq. (3) solely to the inputs  $\mathcal{X}$  is insufficient to fully block the confounding effects [49]. Therefore, we implement continuous intervention in both stages of front-door path [37], *i.e.*, by simultaneously applying *do*-operation to  $\mathcal{X}$  and  $\mathcal{M}$ . First, the effect of  $\mathcal{X}$  on  $\mathcal{M}$  is identifiable:

$$P(\mathcal{M}|do(\mathcal{X})) = P(\mathcal{M}|\mathcal{X}). \quad (4)$$

Then, for the second stage  $\mathcal{M} \rightarrow \mathcal{Y}$ , we apply the adjustment formulation and have:

$$P(\mathcal{Y}|do(\mathcal{M})) = \sum_{x'} P(\mathcal{Y}|\mathcal{M}, x')P(x'). \quad (5)$$

Here,  $x'$  denotes potential inputs of the whole representation space, different from current inputs  $\mathcal{X} = x$ . To chain together these two partial effects to obtain the overall effect of  $\mathcal{X}$  on  $\mathcal{Y}$ , we sum over all states  $m$  of  $\mathcal{M}$  to form overall front-door adjustment as follow:

$$P(\mathcal{Y}|do(\mathcal{X})) = \sum_m P(\mathcal{Y}|do(m))P(m|do(\mathcal{X})) \quad (6)$$

$$= \sum_{x'} P(x') \sum_m P(\mathcal{Y}|m, x')P(m|\mathcal{X}). \quad (7)$$

From the above derivation, we can observe that the front-door adjustment in causal inference involves the intermediate knowledge of current input  $\mathcal{X} = x$  (*i.e.*, the current features) as well as the cross-sampling features of other samples from the entire training set. We utilize the bold symbol  $\mathbf{m}$  and  $\mathbf{x}'$  to represent these two components respectively.

Here, the intermediate knowledge is extracted from current input  $\mathbf{m} \sim x$ . Detailed methods for sampling  $\mathbf{x}'$  are introduced in subsequent sections.

For convenience, we define the network module as a linear function  $f(x, \mathbf{x}')$  to model the computation of  $x$  and  $\mathbf{x}'$  to obtain  $\mathcal{Y}$ . Meanwhile, according to the Bayes' rule and the definition of Expected values, the front-door adjustment  $\mathcal{FD}(\cdot)$  of Eq. (7) can be expressed as:

$$P(\mathcal{Y}|do(\mathcal{X})) = \mathcal{FD}(x, \mathbf{x}') \quad (8)$$

$$= \mathbb{E}_{x'} \mathbb{E}_{\mathbf{m}|x} [f(x, \mathbf{x}')], \quad (9)$$

where the linear function is used as  $f(x, \mathbf{x}') = f_x(x) + f_{x'}(\mathbf{x}')$ . Hence, based on the linear mapping model, the Eq. (9) can be formulated as  $\mathbb{E}_{x'}[\mathbf{x}'] + \mathbb{E}_{\mathbf{m}|x}[\mathbf{m}]$ . Since the closed-form solution of expected values are difficult to obtain in the complex representation space [49], we employ the query mechanism to achieve the estimation:

$$\mathbb{E}_{x'}[\mathbf{x}'] \approx \sum_{x'} P(\mathbf{x}'|g_1)x' = \sum_i \frac{\exp(g_1 \mathbf{x}_i^{T'})}{\sum_j \exp(g_1 \mathbf{x}_j^{T'})} \mathbf{x}_i' \quad (10)$$

$$\mathbb{E}_{\mathbf{m}|x}[\mathbf{m}] \approx \sum_m P(\mathbf{m}|g_2)\mathbf{m} = \sum_i \frac{\exp(g_2 \mathbf{m}_i^T)}{\sum_j \exp(g_2 \mathbf{m}_j^T)} \mathbf{m}_i, \quad (11)$$

where  $g_1 = q_1(x)$  and  $g_2 = q_2(x)$  are two embedding functions [32, 54] that transmit input  $x$  into two query sets. Then, the front-door adjustment  $\mathcal{FD}(\cdot)$  is approximated as follows:

$$\mathcal{FD}(x, \mathbf{x}') = \mathbb{E}_{x'}[\mathbf{x}'] + \mathbb{E}_{\mathbf{m}|x}[\mathbf{m}]. \quad (12)$$

As we realize an approximate estimation through a query mechanism, multi-head attention [46] can be efficiently employed to handle the aforementioned process.

**Specific Network Design.** Although the derivation is clear, how to implement the causal inference in networks presents a significant technical challenge. Considering the characteristics of COPE, we propose leveraging the keypoint features of object as the intermediate knowledge  $\mathbf{m}$ , since the keypoints that are evenly distributed on the surface can effectively capture structure and pose information of the object. Specifically, with the fusion input feature  $\mathcal{F}_{obj}$ , we detect  $N_{kpt}$  local keypoints and perform global information aggregation to extract features  $\mathcal{F}_{kpt} \in \mathbb{R}^{N_{kpt} \times C}$ , following previous keypoint-based methods [25, 28]. As for the cross-sampling features  $\mathbf{x}'$ , one straightforward way is to construct a memory bank of all features and randomly sample a certain number of features from it as the cross-sampling features. Afterward, the memory bank is updated at the corresponding positions using the features from the current mini-batch [52]. However, this intuitive approach is not applicable to our task, since the memory bank should cover all samples, it may not capture the dynamic variations of features during training. The lack of feature consistency could introduce additional confounders, which will negatively impact the models to focus on correct causal relations.

To this end, we draw inspiration from MoCo [11] and devise a features sampling approach based on a dynamic queue. Specifically, we first utilize the 3D encoders of ULIP-2 [53] to extract a specified number of features for each category, constructing an initial 2D queue with a shape of  $N_c \times N_q$ , where  $N_c$  and  $N_q$  represent the number of categories and the queue length of each category, respectively. Next, we randomly sample  $N_s$  features from the queue to form  $\mathbf{x}'$ , which is denoted as  $\mathcal{F}_{samp} \in \mathbb{R}^{N_s \times C}$  in the networks. Based on the queue's characteristics, we update the keypoint features  $\mathcal{F}_{kpt}$  from the current epoch into the queue via first-in-first-out (FIFO) approach, ensuring feature consistency within the queue. Following Eq. (10) to Eq. (12), the causality-enhanced features  $\mathcal{F}_f$  are obtained as follow:

$$\mathcal{F}_s = SA(\mathcal{F}_{kpt}), \mathcal{F}_c = CA(\mathcal{F}_{kpt}, \mathcal{F}_{samp}) \quad (13)$$

$$\mathcal{F}_f = LN(\mathcal{F}_s + \mathcal{F}_c), \quad (14)$$

where  $SA(\cdot)$  and  $CA(\cdot)$  represent multi-head self-attention and cross-attention, respectively.  $LN(\cdot)$  denotes the layer normalization. Furthermore, to strengthen the stability of learning by fusing causality-enhanced features with original keypoint features of objects, we introduce an adaptive weight fusion method:

$$w_a = \sigma(\mathcal{F}_f W_f + \mathcal{F}_{kpt} W_k) \quad (15)$$

$$\mathcal{F}_f \leftarrow w_a \odot \mathcal{F}_f + (1 - w_a) \odot \mathcal{F}_{kpt}, \quad (16)$$

where  $\sigma$  and  $\odot$  mean Sigmoid function and element-wise multiplication. Suppose  $W_{f/k} \in \mathbb{R}^{C \times 1}$  is learnable weight parameter.

### 4.3. Category Knowledge Distillation

As mentioned in above section, implicitly learning category knowledge from a limited dataset only results in limited intra-category generalization. Inspired by the feature alignment design [14, 65, 66] to transfer visual-language knowledge to different tasks, we propose a modified residual approach to distill the category knowledge from 3D foundation models into COPE network, as shown in Fig. 3(c). Unlike CLIPose [26] exploits contrastive learning to extract semantic knowledge from text and image modalities, we leverage the pre-trained 3D encoder in ULIP-2 [53], which possesses strong awareness of point cloud structures and category information. Specifically, given the input point cloud of a object  $\mathcal{P}_{obj}$ , we can directly feed it into the frozen 3D Encoder  $\Phi_{ULIP}$  of ULIP-2, which can be written as:

$$\mathcal{F}_P^{ULIP} = \Phi_{ULIP}(\mathcal{P}_{obj}), \quad (17)$$

where  $\mathcal{F}_P^{ULIP} \in \mathbb{R}^{1 \times C_3}$  denotes the [CLS] token in Point Transformer. The feature of [CLS] token embeds representation of the whole point cloud. To obtain the representation of our model, we employ a simple average pooling on point features and get  $\mathcal{F}_P^{avg} \in \mathbb{R}^{1 \times C_1}$ , we have:

$$\mathcal{F}_P^{avg} = \text{AvgPool}(\mathcal{F}_P). \quad (18)$$

Then, we apply a modified residual distillation network on  $\mathcal{F}_P^{avg}$  to transform with two MLP projectors  $K_1$  and  $K_2$ :

$$\widehat{\mathcal{F}}_P^{avg} = \mathcal{F}_P^{avg} + \mu \times K_2(\delta(K_1(\mathcal{F}_P^{avg}))), \quad (19)$$

where  $K_{1/2} \in \mathbb{R}^{C_1 \times C_1}$ ,  $\delta$  represents GELU function and  $\mu$  is a balancing parameter. Moreover, we initialize the parameters of the second layer  $K_2$  as zeros. Therefore,  $\widehat{\mathcal{F}}_P^{avg}$  initially contains only  $\mathcal{F}_P^{avg}$  and is gradually updated, which avoids introducing additional confounders. Lastly, we can utilize L2 loss to supervise the category knowledge distillation:

$$\mathcal{L}_{KD} = \frac{1}{B} \sum_i^B \left\| \mathcal{F}_P^{ULIP} - \psi(\widehat{\mathcal{F}}_P^{avg}) \right\|_2, \quad (20)$$

where  $\psi \in \mathbb{R}^{C_1 \times C_3}$  is a learnable embedding layer and  $B$  denotes the batch size. In this way, the tuned point cloud features of our model can effectively receive supervision from generalized ones, facilitating comprehensive category knowledge learning and enhancing the model’s intra-category generalization.

#### 4.4. Pose Estimation and Overall Loss Function

With the obtained causality-enhanced features, following previous works [22, 25], we recover the final pose and size  $\mathcal{R}, t, s$  via set of keypoint-level correspondences containing global features and points. A simply L1 Loss is used to supervise the predicted pose, in formula:

$$\mathcal{L}_{pose} = \|\mathcal{R}_{gt} - \mathcal{R}\|_2 + \|t_{gt} - t\|_2 + \|s_{gt} - s\|_2, \quad (21)$$

where  $\mathcal{R}_{gt}, t_{gt}, s_{gt}$  means the ground truth rotation, translation and size. For more details please refer to supplementary or [25]. Hence, the overall loss function is as follow:

$$\mathcal{L}_{all} = \alpha_1 \mathcal{L}_{pose} + \alpha_2 \mathcal{L}_{KD}, \quad (22)$$

where  $\alpha_1, \alpha_2$  are hyper-parameters to balanced the contribution of each term. We omit some loss terms for brevity. *Please see supplementary for more details.*

## 5. Experiments

**Datasets.** Following previous works [4, 23, 25, 26, 63], we conduct experiments not only on two mainstream NOCS benchmarks, REAL275 [48] and CAMERA25 [48] as well as HouseCat6D [17] datasets. REAL275 is a challenge real-world dataset that contains objects from 6 categories. The training data consists of 4.3k images from 7 scenes, while testing data includes 2.75k from 6 scenes and 3 objects from each category. CAMERA25 is a synthetic dataset that obtains the same categories as REAL275. It provides 300k synthetic RGB-D images of objects rendered on virtual background, with 25k images are withhold for testing. HouseCat6D is a comprehensive multi-modal real-world dataset and encompasses 10 household categories. The training set consists of 20k frames from 34 scenes and

testing set consists of 3k frames across 5 scenes. With a total of 194 objects, each category contains 19 objects on average.

**Evaluation Metrics.** Following [4, 25], we evaluate the model performance with two metrics. **(i) 3D IoU.** As for NOCS dataset, we report mean average precision (mAP) of CATRE [31] Intersection over Union (IoU) with the thresholds of 75%. For the HouseCat6D dataset, we report the mAP of 3D IoU under thresholds of 25% and 50%. **(ii) n°m cm.** We also utilize the combination of rotation and translation metrics of  $5^\circ 2\text{ cm}$ ,  $5^\circ 5\text{ cm}$ ,  $10^\circ 2\text{ cm}$  and  $10^\circ 5\text{ cm}$ , which means the estimation is considered correct when the error is below a threshold.

**Implementation Details.** For a fair comparison, we utilize the same segmentation masks as AG-Pose [25] and DPDN [22] from MaskRCNN [10] and resize them to  $224 \times 224$ . For model parameters, the feature dimensions are set as  $C_1 = C_2 = 128$ ,  $C_3 = 768$  and  $C = 256$ , respectively. The number of point  $N$  in point cloud is 1024 and the number of keypoints  $N_{kpt}$  is set as 96. In dynamic queue, we set the size of queue  $N_q$  to 80 and randomly select  $N_s = 12$  features. For the use of pre-trained 3D models of ULIP-2, we apply PointBert [56] for knowledge distillation and employ PointNet++ [40] for queue construction. For the hyper-parameters setting, the balancing parameter  $\mu$  in residual network is set as 0.1 following [14], and  $\alpha_1, \alpha_2$  in overall loss function are 1 and 0.01, respectively. For model optimizing, we employ the same data augmentation approach as previous works [22, 25], which leverage random rotation degree sampled from  $U(0, 20)$  and rotation  $\Delta t \sim U(-0.02, 0.02)$  and scaling  $\Delta s \sim U(-0.18, 1.2)$ . The network is training on a single NVIDIA L40 GPU for a total of 120k iterations by the Adam [18] optimizer, with a mini training batch is 24 and a learning rate range from  $2e-5$  to  $5e-4$  based on triangular2 cyclical schedule [42].

### 5.1. Comparison with State-of-the-Art Methods

As shown in Fig. 4, our method outperforms existing sota methods across multiple key metrics in different datasets.

**Performance on REAL275 dataset.** The comparisons between proposed CleanPose and previous methods on challenging REAL275 dataset are shown in Tab. 1. As can be easily observed, our CleanPose achieves the state-of-the-art performance in all metrics and outperforms all previous methods on REAL275 dataset. Significantly, we achieve the precision of **61.5%**, **67.4%** and **78.3%** in the rigorous metric of  $5^\circ 2\text{ cm}$ ,  $5^\circ 5\text{ cm}$  and  $10^\circ 2\text{ cm}$ , surpassing the current state-of-the-art method AG-Pose<sup>1</sup> [25] with a large margin by 4.5%, 2.8% and 3.2%, respectively. Moreover, the qualitative results of AG-Pose and proposed CleanPose

<sup>1</sup>Throughout the comparison in all experiments, we use the result suggested by the AG-Pose [25] official implementation, which is higher than reported result in the original paper.

Methods	Venue/Source	$IoU_{75}^*$ ↑	$5^\circ 2cm$ ↑	$5^\circ 5cm$ ↑	$10^\circ 2cm$ ↑	$10^\circ 5cm$ ↑
SPD[43]	ICCV'20	27.5	19.3	21.4	43.2	54.1
DualPoseNet[21]	ICCV'21	30.8	29.3	35.9	50.0	66.8
GPV-Pose[5]	CVPR'22	23.1	32.5	43.3	58.2	76.6
6D-ViT[67]	TIP'22	33.3	38.2	41.9	59.1	67.9
HS-Pose[62]	CVPR'23	39.1	45.3	54.9	68.6	83.6
IST-Net[28]	ECCV'23	-	47.8	55.1	69.5	79.6
VI-Net[23]	ICCV'23	48.3	50.0	57.6	70.8	82.1
CLIPose[26]	TCSVT'24	-	48.5	58.2	70.3	85.1
GenPose[58]	NeurIPS'23	-	52.1	60.9	72.4	84.0
HS + GeoReF[63]	CVPR'24	54.3	51.7	59.6	74.3	83.3
SPD + GeoReF[63]	CVPR'24	51.8	54.4	60.3	71.8	79.4
MH6D[29]	TNNLS'24	54.2	53.0	61.1	72.0	82.0
SecondPose[4]	CVPR'24	49.7	56.2	63.6	74.7	<u>86.0</u>
AG-Pose[25]	CVPR'24	61.3	<u>57.0</u>	<u>64.6</u>	<u>75.1</u>	84.7
<b>CleanPose (ours)</b>		<b>62.6</b>	<b>61.5</b>	<b>67.4</b>	<b>78.3</b>	<b>86.2</b>

Table 1. Comparisons with state-of-the-art methods on REAL275 dataset. ↑: a higher value indicating better performance. ‘\*’ denotes CATRE [31] IoU metrics and ‘-’ means unavailable statistics. Overall best results are in **bold** and the second best results are underlined.

Methods	$IoU_{75}^*$	$5^\circ 2cm$	$5^\circ 5cm$	$10^\circ 2cm$	$10^\circ 5cm$
SPD[43]	-	54.3	59.0	73.3	81.5
DualPoseNet[21]	-	64.7	70.7	77.2	84.7
SGPA[1]	-	70.7	74.5	82.7	88.4
HS-Pose[62]	-	73.3	80.5	80.4	89.4
CLIPose[26]	-	74.8	82.2	82.0	91.2
GeoReF[63]	79.2	77.9	<u>84.0</u>	83.8	90.5
AG-Pose[25]	<u>81.2</u>	<u>79.5</u>	83.7	<u>87.1</u>	<u>92.6</u>
<b>CleanPose (ours)</b>	<b>80.7</b>	<b>80.3</b>	<b>84.2</b>	<b>87.7</b>	<b>92.7</b>

Table 2. Comparisons with state-of-the-art methods on CAMERA25 dataset. A higher value indicating better performance. ‘\*’ denotes CATRE [31] IoU metrics and ‘-’ means unavailable statistics. Overall best results are in **bold** and the second best results are underlined.

Methods	$IoU_{25}$	$IoU_{50}$	$5^\circ 2cm$	$5^\circ 5cm$	$10^\circ 2cm$	$10^\circ 5cm$
FS-Net[2]	74.9	48.0	3.3	4.2	17.1	21.6
GPV-Pose[5]	74.9	50.7	3.5	4.6	17.8	22.7
VI-Net[23]	80.7	56.4	8.4	10.3	20.5	29.1
SecondPose[4]	83.7	66.1	11.0	13.4	25.3	35.7
AG-Pose[25]	<u>88.1</u>	<u>76.9</u>	<u>21.3</u>	<u>22.1</u>	<u>51.3</u>	<u>54.3</u>
<b>CleanPose (ours)</b>	<b>89.2</b>	<b>79.8</b>	<b>22.4</b>	<b>24.1</b>	<b>51.6</b>	<b>56.5</b>

Table 3. Comparisons with state-of-the-art methods on HouseCat6D dataset. A higher value indicating better performance. Overall best results are in **bold** and the second best results are underlined.

are shown in Fig. 5. It can be observed that our method achieves significantly higher precision. These exceptional outcomes further support the efficacy of our approach.

**Performance on CAMERA25 dataset.** The results comparison of our method and the state-of-the-art is presented in Tab. 2. From the observation of results, it can be deduced that CleanPose ranks top performance across all the metrics

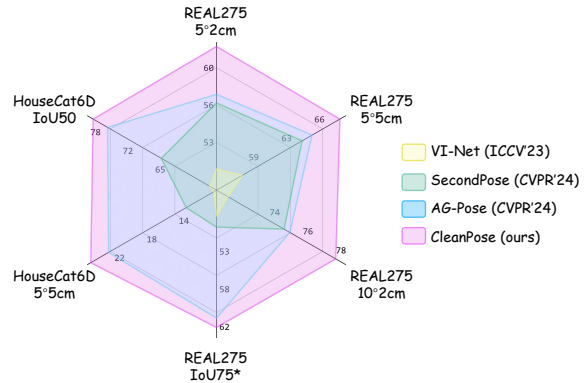


Figure 4. Comparison of CleanPose with sota methods.

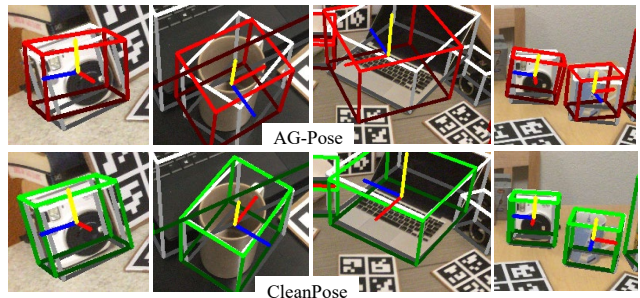


Figure 5. Qualitative comparison on REAL275 [48]. We compare the predictions of CleanPose and the baseline AG-Pose [25]. The ground truth is marked by white borders.

except  $IoU_{75}$ , in which our method also achieves comparable performance with the best (80.7% vs. 81.2%). In detail, the proposed CleanPose achieves 80.3% on  $5^\circ 2cm$ , 84.2% on  $5^\circ 5cm$ , 87.7% on  $10^\circ 2cm$  and 92.7% on  $10^\circ 5cm$ , respectively. This superior performance on synthetic dataset further proves the effectiveness of our method.

**Performance on HouseCat6D dataset.** In Tab. 3, we eval-

ID	Causal	Distillation	5°2cm	5°5cm	10°2cm	10°5cm
1	✗	✗	57.0	64.6	75.1	84.7
2	✓	✗	59.7	66.5	77.9	85.1
3	✗	✓	58.9	66.1	76.3	85.9
4	✓	✓	<b>61.5</b>	<b>67.4</b>	<b>78.3</b>	<b>86.2</b>

Table 4. Effect of causal learning and knowledge distillation.

Data	Update	5°2cm	5°5cm	10°2cm	10°5cm
Queue	FIFO	<b>61.5</b>	<b>67.4</b>	<b>78.3</b>	<b>86.2</b>
Queue	w/o update	57.1	63.1	77.5	85.7
Queue	Similarity	59.1	65.8	77.6	86.0
Memory bank	w/o update	57.6	64.4	75.6	83.8
Memory bank	Similarity	58.1	65.4	77.5	86.1

(a) Effect of different feature storage methods and update strategies.

	5°2cm	5°5cm	10°2cm	10°5cm
w/o fusion	58.5	65.2	<b>79.0</b>	<b>86.5</b>
w/ fusion	<b>61.5</b>	<b>67.4</b>	78.3	86.2

(b) Effect of adaptive weight fusion in front-door adjustment.

Policies	5°2cm	5°5cm	10°2cm	10°5cm
Contrastive	55.3	63.1	76.2	86.0
MLP	56.4	63.1	77.6	85.9
MLP + residual	<b>61.5</b>	<b>67.4</b>	<b>78.3</b>	<b>86.2</b>

(c) Effect of distinct feature distillation policies.

3D Encoder	5°2cm	5°5cm	10°2cm	10°5cm
PointNet++[40]	57.6	65.3	75.0	84.4
PointMLP[33]	57.0	64.3	77.4	<b>86.2</b>
PointBert[56]	<b>61.5</b>	<b>67.4</b>	<b>78.3</b>	<b>86.2</b>

(d) Effect of different 3D encoders of ULIP-2 [53] for distillation.

Table 5. Ablation studies on key details. Default settings are colored in gray .

uate our method on HouseCat6D [17] dataset. The proposed CleanPose again achieves state-of-the-art performance in all metrics. In detail, our method outperforms the current best method AG-Pose [25] by 2.9% on  $IoU_{50}$ , 1.1% on 5°2 cm, 2.0% on 5°5 cm and 2.1% on 10°5 cm, respectively. The overall and category-wise evaluation of 3D IoU on HouseCat6D dataset is provided in *supplementary material*.

## 5.2. Ablation Studies

We conduct ablation experiments to demonstrate the effectiveness of the proposed method on the REAL275 dataset [48].

### Effect of Causal Learning and Knowledge Distillation.

In Tab. 4, we perform ablations of the proposed two main components. We adopt AG-Pose [25] as our baseline, which serves as the current sota framework in COPE. The results indicate that the integration of causal inference or knowledge distillation leads to significant enhancements in the

model’s performance. This strongly demonstrates causal learning’s considerable potential and the effectiveness of comprehensive category information guidance in COPE.

### Effect of different feature storage methods and update strategies.

In Tab. 5a, we investigate the impact of distinct combinations of feature storage and update strategies. “Similarity” represents updating the closest features via similarity computation. The results indicate that employing the dynamic queue and FIFO update mechanism yields the best performance. We owe the advantage to the dynamic queue’s superior ability to capture feature variations compared to a memory bank. Moreover, the FIFO mechanism ensures the removal of outdated features, which is beneficial for causal inference.

### Effect of adaptive weight fusion method.

As shown in Tab. 5b, our model achieves sota performance even without feature fusion. Introduction of the adaptive feature fusion method further improves the results in rigorous metrics.

### Effect of distinct feature distillation policies.

In Tab. 5c, we assess the impact of distinct feature distillation policies. The contrastive learning minimizes the feature distance via feature alignment. Our proposed residual distillation policy achieves the best performance since the residual layers effectively balance feature learning and knowledge transfer.

### Effect of different 3D encoders.

Tab. 5d illustrates the impact of using different 3D encoders in the distillation. Objectively, the pre-trained PointBert [56] realizes the sota point cloud zero-shot classification results [53]. Our model is also more performant using PointBert. It is noteworthy that using PointNet++ [40], which serves as the feature extractor in our model, does not achieve the best performance. This further demonstrates that our proposed knowledge distillation network focuses on category knowledge rather than feature similarity. *Please see supplementary for more ablations.*

## 6. Conclusion

In this paper, we present CleanPose, the first solution that addresses the confounders in category-level pose estimation from the perspective of causal learning. Motivated by pivotal observation that humans can learn inherent causality beyond biases, we develop a causal inference framework based on front-door adjustment. We formulate the modeling of crucial causal variables in pose estimation task. Guided by the causal modeling, we devise an effective data sampling method and a adaptive feature fusion module to achieve unbiased estimation. Furthermore, we propose a residual knowledge distillation network to transfer rich 3D category information, providing comprehensive category-specific guidance. Extensive experiments on challenging benchmarks REAL275, CAMERA25 and HouseCat6D demonstrate that CleanPose can significantly improve performance, showing the effectiveness of our method.



# CleanPose: Category-Level Object Pose Estimation via Causal Learning and Knowledge Distillation

## Supplementary Material

### A. Limitation and Broader Impact

**Limitation and future work.** While our method achieves superior results in various challenging benchmarks of category-level pose estimation, there are still several aspects for improvement. First, although the front-door adjustment is effective, the investigate on the application of causal learning methods remains incomplete. Therefore, exploring further use of different causal learning methods such as back-door adjustment and counterfactual reasoning may enhance the performance of CleanPose. Second, despite the guidance of the causal analysis, the network modules in actual implementation may induce inaccuracy inevitably. Such a flaw introduces a gap between the causal framework and the network design. In future work, we will further study advanced algorithm design strategies.

**Broader Impact.** For tasks with parameter regression properties, *e.g.*, category-level pose estimation, the current mainstream approaches focus on exploring advanced network designs to perform data fitting. We believe that relying solely on learning statistical similarity can also introduce spurious correlations into parameter regression models, thereby damaging the model’s generalization ability. We hope this work brings new insights for the broader and long-term research on parameter regression tasks. Besides, adapting foundation models to downstream tasks has become a dominant paradigm in machine learning. Our method also provide novel views for offering knowledge guidance in similar tasks across diverse categories.

### B. More Loss Function Details

The backbone of our method is based on AG-Pose [25]. In addition to  $\mathcal{L}_{pose}$  (Eq. (21)), there are some additional loss functions to balance keypoints selection and pose prediction. First, to encourage the keypoints to focus on different parts, the diversity loss  $\mathcal{L}_{div}$  is used to force the detected keypoints to be away from each other, in detail:

$$\mathcal{L}_{div} = \sum_{i=1}^{N_{kpt}} \sum_{j=1, j \neq i}^{N_{kpt}} \mathbf{d}(\mathcal{P}_{kpt}^{(i)}, \mathcal{P}_{kpt}^{(j)}) \quad (23)$$

$$\mathbf{d}(\mathcal{P}_{kpt}^{(i)}, \mathcal{P}_{kpt}^{(j)}) = \max \left\{ th_1 - \left\| \mathcal{P}_{kpt}^{(i)} - \mathcal{P}_{kpt}^{(j)} \right\|_2, 0 \right\}, \quad (24)$$

where  $th_1$  is a hyper-parameter and is set as 0.01,  $\mathcal{P}_{kpt}^{(i)}$  means the  $i$ -th keypoint. To encourage the keypoints to locate on the surface of the object and exclude outliers simultaneously, an object-aware chamfer distance loss  $\mathcal{L}_{ocd}$

is employed to constrain the distribution of  $\mathcal{P}_{kpt}$ . In formula:

$$\mathcal{L}_{ocd} = \frac{1}{|\mathcal{P}_{kpt}|} \sum_{x_i \in \mathcal{P}_{kpt}} \min_{y_j \in \mathcal{P}'_{obj}} \|x_i - y_j\|_2, \quad (25)$$

where  $\mathcal{P}'_{obj}$  denotes the point cloud of objects without outlier points. Moreover, we also use MLP to predict the NOCS coordinates of keypoints  $\mathcal{P}_{kpt}^{nocs} \in \mathbb{R}^{N_{kpt} \times 3}$ .

Then, we generate ground truth NOCS of keypoints  $\mathcal{P}_{kpt}^{gt}$  by projecting their coordinates under camera space  $\mathcal{P}_{kpt}$  into NOCS using the ground truth  $\mathcal{R}_{gt}, t_{gt}, s_{gt}$ . And we use the *SmoothL1* loss to supervise the NOCS projection:

$$\mathcal{P}_{kpt}^{gt} = \frac{1}{\|s_{gt}\|_2} \mathcal{R}_{gt} (\mathcal{P}_{kpt} - t_{gt}) \quad (26)$$

$$\mathcal{L}_{nocs} = \text{SmoothL1}(\mathcal{P}_{kpt}^{gt}, \mathcal{P}_{kpt}^{nocs}). \quad (27)$$

Hence, the complete form of overall loss (Eq. (22)) is as follows:

$$\mathcal{L}_{all} = \lambda_1 \mathcal{L}_{ocd} + \lambda_2 \mathcal{L}_{div} + \lambda_3 \mathcal{L}_{nocs} + \lambda_4 \mathcal{L}_{pose} + \alpha_2 \mathcal{L}_{KD}, \quad (28)$$

where the parameters are set as  $(\lambda_1, \lambda_2, \lambda_3, \lambda_4, \alpha_2) = (1.0, 5.0, 1.0, 0.3, 0.01)$  according to AG-Pose [25] and following ablations.

### C. More Details of Using ULIP-2

ULIP-2 [53] is a large-scale 3D foundation model with strong perception capabilities for the point cloud modality. It offers multiple pre-trained versions of point cloud encoders. In our model, there are two key steps that involve the use of different pre-trained encoders of ULIP-2. **(i)** In the knowledge distillation process, we leverage the pre-trained PointBert [56], which achieves the best zero-shot classification performance across all versions. Therefore, it can provide comprehensive category knowledge guidance for our model. In the ablation study Tab. 5d, we also compared it with PointNet++ [40], which is more similar in architecture to our model. The experimental results demonstrate that our distillation method focuses more on category knowledge rather than feature similarity. **(ii)** However, during the initial construction of the dynamic queue, we use the pre-trained PointNet++ [40], as the front-door adjustment primarily focuses on the differences between samples. We aim to avoid introducing confounders due to feature discrepancies from different encoders. The additional ablation study results in Tab. 7b also support our analysis.

$N_q$	5°2cm	5°5cm	10°2cm	10°5cm
20	57.0	64.6	75.1	84.7
50	60.5	66.5	77.9	<b>86.4</b>
<b>80</b>	<b>61.5</b>	<b>67.4</b>	<b>78.3</b>	86.2
200	59.4	66.1	78.0	85.9
500	58.8	65.3	76.8	85.8
1000	58.3	66.8	76.3	86.2
3000	57.7	65.5	75.6	85.0
10000	57.0	65.0	75.7	85.4

(a) Effect of varying queue lengths  $N_q$ 

$N_s$	5°2cm	5°5cm	10°2cm	10°5cm
6	59.4	65.3	76.8	84.3
<b>12</b>	<b>61.5</b>	<b>67.4</b>	78.3	86.2
18	58.7	65.5	<b>78.8</b>	<b>86.8</b>
24	58.5	64.8	77.8	85.9
48	56.8	64.5	76.3	85.6
80	56.9	64.4	76.2	85.8

(b) Effect of varying queue lengths  $N_s$ 

$\alpha_2$	5°2cm	5°5cm	10°2cm	10°5cm
0.005	59.3	66.8	78.0	<b>87.4</b>
<b>0.01</b>	<b>61.5</b>	<b>67.4</b>	<b>78.3</b>	86.2
0.1	58.4	65.1	77.6	85.9
0.5	57.3	63.9	76.2	86.0
1	56.9	63.4	76.4	85.4

(c) Effect of varying balanced coefficient  $\alpha_2$ 

Table 6. Additional ablation studies on some hyper-parameters. Default settings are colored in gray .

## D. Additional Ablations

**Effect of varying queue lengths  $N_q$ .** Tab. 6a ablates the different lengths of dynamic queue  $N_q$ . The queue that is too short results in insufficient sample diversity, while too long affect memory efficiency and feature consistency. We observe that the estimation performance achieves the peak at the length of around 80, with slight declines upon further increases. We speculate that the queue length is closely related to task characteristics and data scale of COPE. We select  $N_q = 80$  in our model to balance between efficiency and accuracy.

**Effect of different sampling quantities  $N_s$ .** In Sec. 4.2 of main manuscript, we sample  $N_s$  features for the specific network design to perform *front-door adjustment*. We study the influence with response to different sampling quantities  $N_s$  in Tab. 6b. We find that a large  $N_s$  leads to a slight performance degradation as selected features may not capture the representation space properly. The results demonstrate that  $N_s = 12$  yields the most significant performance gains.

**Varying balanced coefficient  $\alpha_2$  for loss  $\mathcal{L}_{KD}$ .** In Sec. 4.3 of main manuscript, we introduce L2 loss to supervise the

Init.	5°2cm	5°5cm	10°2cm	10°5cm
Random	57.0	65.7	74.8	85.4
Extract	<b>61.5</b>	<b>67.4</b>	<b>78.3</b>	<b>86.2</b>

(a) Effect of different queue initialization approaches

3D Encoder	5°2cm	5°5cm	10°2cm	10°5cm
PointNet++[40]	<b>61.5</b>	<b>67.4</b>	<b>78.3</b>	86.2
PointMLP[33]	56.1	64.8	76.0	85.2
PointBert[56]	58.8	65.2	77.9	<b>86.4</b>

(b) Effect of different 3D encoders of ULIP-2 [53] for initial construction of the queue.

Selector	5°2cm	5°5cm	10°2cm	10°5cm
Random	<b>61.5</b>	<b>67.4</b>	<b>78.3</b>	86.2
K-means	58.5	65.1	78.0	<b>86.5</b>
K-means (simi)	56.7	64.2	76.7	86.0

(c) Effect of distinct feature selectors

Table 7. Additional ablation studies on confounders queue. Default settings are colored in gray .

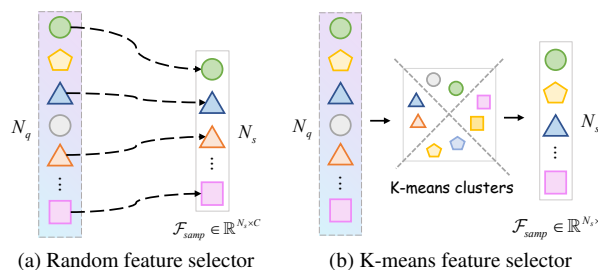


Figure 6. Illustration of different feature selectors in ablations Tab. 7c.

feature-based distillation and use  $\alpha_2$  to balanced its contribution in overall loss function. We investigate the impact of different  $\alpha_2$  in Tab. 6c. We observe that the better performance is achieved when  $\alpha_2$  is small, possibly because  $\mathcal{L}_{KD}$  is comparable in magnitude to the pose loss function, which is favorable for regression. The results show that our method performs well under  $\alpha_2 = 0.01$ .

**Different queue initialization approaches.** By default, we construct confounders queue with features extracted by 3D encoders of ULIP-2 [53]. Alternatively, we can randomly initialize the queue, which should achieve the same effect ideally. Therefore, we evaluate the performance between two initialization approaches in Tab. 7a. The results indicate the degraded performance with “Random” initialization strategy. We speculate that the randomly initialized queue may introduce additional and uncontrollable confounders, limiting the model’s optimization potential.

**Effect of different 3D encoder for initial construction of the queue.** Tab. 7b ablates the different 3D encoders of

Category	$IoU_{25}^*$	$IoU_{50}^*$	$IoU_{75}^*$	$5^\circ 2cm$	$5^\circ 5cm$	$10^\circ 2cm$	$10^\circ 5cm$
bottle	51.3	49.4	36.9	75.3	81.7	79.9	87.8
bowl	100.0	100.0	93.8	92.8	97.8	95.0	99.9
camera	90.9	83.5	39.5	2.8	3.1	33.9	40.5
can	71.3	71.1	43.1	84.2	85.8	96.9	98.6
laptop	86.3	84.0	76.1	68.9	90.2	71.9	98.5
mug	99.6	99.4	86.1	45.3	45.6	91.9	91.9
Average	83.3	81.2	62.6	61.5	67.4	78.3	86.2

Table 8. Category-wise evaluation of CleanPose on REAL275 dataset. ‘\*’ denotes CATRE [31] IoU metrics.

Methods	$IoU_{75}\uparrow$	$IoU_{25}/IoU_{50}\uparrow$										
		Average	Bottle	Box	Can	Cup	Remote	Teapot	Cutlery	Glass	Tube	Shoe
NOCS[48]	-	50.0/21.2	41.9/5.0	43.3/6.5	81.9/62.4	68.8/2.0	<b>81.8/59.8</b>	24.3/0.1	14.7/6.0	95.4/49.6	21.0/4.6	26.4/16.5
FS-Net[2]	14.8	74.9/48.0	65.3/45.0	31.7/1.2	98.3/73.8	96.4/68.1	65.6/46.8	69.9/59.8	71.0/51.6	99.4/32.4	79.7/46.0	71.4/55.4
GPV-Pose[5]	15.2	74.9/50.7	66.8/45.6	31.4/1.1	98.6/75.2	96.7/69.0	65.7/46.9	75.4/61.6	70.9/52.0	99.6/62.7	76.9/42.4	67.4/50.2
VI-Net[23]	20.4	80.7/56.4	90.6/79.6	44.8/12.7	<u>99.0/67.0</u>	96.7/72.1	54.9/17.1	52.6/47.3	89.2/76.4	99.1/93.7	<b>94.9/36.0</b>	85.2/62.4
SecondPose[4]	24.9	83.7/66.1	94.5/79.8	<b>54.5/23.7</b>	<u>98.5/93.2</u>	<u>99.8/82.9</u>	53.6/35.4	81.0/71.0	93.5/74.4	99.3/92.5	75.6/35.6	86.9/73.0
AG-Pose[25]	<u>53.0</u>	88.1/76.9	<u>97.6/86.0</u>	<u>54.0/13.9</u>	<u>98.3/96.7</u>	<b>100/99.9</b>	53.9/37.2	<b>99.9/98.5</b>	<u>96.0/93.3</u>	<u>100/99.3</u>	81.4/45.0	<u>99.7/99.5</u>
<b>CleanPose</b>	<b>53.9</b>	<b>89.2/79.8</b>	<b>99.9/79.1</b>	51.4/ <b>28.7</b>	<b>99.9/99.7</b>	<b>100/99.9</b>	<u>71.2/57.8</u>	<u>99.0/94.0</u>	<b>97.8/91.0</b>	<b>100/99.6</b>	<b>72.7/48.4</b>	<b>99.8/99.8</b>

Table 9. Overall and category-wise evaluation of 3D IoU on the HouseCat6D.  $\uparrow$ : a higher value indicating better performance, ‘-’ means unavailable statistics. Overall best results are in **bold** and the second best results are underlined.

ULIP-2 [53] for initial construction of the dynamic queue. The results exhibit that using PointNet++ [40] yields the most performance gains. As mentioned in Sec. C, the dynamic queue is utilized in the cross-attention phase of front-door adjustment, thus primarily focusing on the differences between samples. Using encoders with similar architectures helps avoid introducing extra confounders.

**Various feature selection strategies.** In Sec. 4.2 of main manuscript, we randomly sample  $N_s$  features from queue by default, as shown in Fig. 6(a). Optionally, we can first use K-means to cluster the features of the queue, and then select features from each cluster to form  $\mathcal{F}_{samp}$ , as illustrated in Fig. 6(b). For fair comparison, the number of clusters is set equal to  $N_s$ . We investigate the impact of these two feature selector in Tab. 7c. As shown in the table, we observe that K-means-based feature sampling strategy shows a decline in performance on strict metrics ( $5^\circ 2cm$  and  $5^\circ 5cm$ ). We argue that k-means, which clusters by Euclidean distance, may lose important boundary information, thus affecting the model performance. Moreover, k-means clustering needs to be performed after each queue update, which increases computational load and training costs. Therefore, we added a comparative experiment using similarity-based updates, denoted as ‘K-means (simi)’, where (simi) refers to the ‘Similarity’ defined in Tab. 5a. In this case, clustering is only performed once during the initial training. However, experimental results also show that such strategy leads to further performance degradation as one clustering loses the diversity of features.

## E. More Experimental Results

We report category-wise results of REAL275 [48] in Tab. 8. Since there is a small mistake in the original evaluation code of NOCS [48] for the 3D IoU metrics, we present more reasonable CATRE [31] metrics following [4, 29, 63]. Further, more detailed results of HouseCat6D [17] are shown in Tab. 9. As for more restricted metric  $IoU_{75}$ , our method also demonstrates state-of-the-art performance (**53.9%**), further validating the effectiveness of CleanPose in 3D IoU evaluation. Moreover, in category-wise validation on  $IoU_{25}$  and  $IoU_{50}$ , our approach obtains state-of-the-art (e.g., *Can*, *Cup*, *Glass* and *Shoe*) or competitive results across all categories. It is worth mentioning that our method exhibits more stable performance on these two metrics. For instance, compared to the current sota method AG-Pose [25] in the *Box* category, our method achieves the best performance (**28.7%**) on  $IoU_{50}$  metric when both obtain competitive results on  $IoU_{25}$  metric, with a significant reduction of the AG-Pose (13.9%).

## References

- [1] Kai Chen and Qi Dou. Sgpa: Structure-guided prior adaptation for category-level 6d object pose estimation. In *Proceedings of the IEEE/CVF International Conference on Computer Vision (CVPR)*, pages 2773–2782, 2021. 7
- [2] Wei Chen, Xi Jia, Hyung Jin Chang, Jinming Duan, Linlin Shen, and Ales Leonardis. Fs-net: Fast shape-based network for category-level 6d object pose estimation with decoupled rotation mechanism. In *Proceedings of the IEEE/CVF*

- Conference on Computer Vision and Pattern Recognition (CVPR)*, pages 1581–1590, 2021. 7, 3
- [3] Xiaozhi Chen, Huimin Ma, Ji Wan, Bo Li, and Tian Xia. Multi-view 3d object detection network for autonomous driving. In *Proceedings of the IEEE conference on Computer Vision and Pattern Recognition (CVPR)*, pages 1907–1915, 2017. 1
- [4] Yamei Chen, Yan Di, Guangyao Zhai, Fabian Manhardt, Chenyangguang Zhang, Ruida Zhang, Federico Tombari, Nassir Navab, and Benjamin Busam. Secondpose: Se (3)-consistent dual-stream feature fusion for category-level pose estimation. In *Proceedings of the IEEE/CVF Conference on Computer Vision and Pattern Recognition (CVPR)*, pages 9959–9969, 2024. 1, 2, 6, 7, 3
- [5] Yan Di, Ruida Zhang, Zhiqiang Lou, Fabian Manhardt, Xiangyang Ji, Nassir Navab, and Federico Tombari. Gpv-pose: Category-level object pose estimation via geometry-guided point-wise voting. In *Proceedings of the IEEE/CVF Conference on Computer Vision and Pattern Recognition (CVPR)*, pages 6781–6791, 2022. 1, 2, 7, 3
- [6] Zhaoxin Fan, Zhengbo Song, Jian Xu, Zhicheng Wang, Kejian Wu, Hongyan Liu, and Jun He. Acr-pose: Adversarial canonical representation reconstruction network for category level 6d object pose estimation. *arXiv preprint arXiv:2111.10524*, 2021. 2
- [7] Yang Fu and Xiaolong Wang. Category-level 6d object pose estimation in the wild: A semi-supervised learning approach and a new dataset. *Advances in Neural Information Processing Systems (NeurIPS)*, 35:27469–27483, 2022. 2
- [8] Xiuye Gu, Tsung-Yi Lin, Weicheng Kuo, and Yin Cui. Open-vocabulary object detection via vision and language knowledge distillation. In *International Conference on Learning Representations (ICLR)*, 2024. 2
- [9] Yang Hai, Rui Song, Jiaojiao Li, and Yinlin Hu. Shape-constraint recurrent flow for 6d object pose estimation. In *Proceedings of the IEEE/CVF Conference on Computer Vision and Pattern Recognition (CVPR)*, pages 4831–4840, 2023. 1
- [10] Kaiming He, Georgia Gkioxari, Piotr Dollár, and Ross Girshick. Mask r-cnn. In *Proceedings of the IEEE International Conference on Computer Vision (CVPR)*, pages 2961–2969, 2017. 3, 6
- [11] Kaiming He, Haoqi Fan, Yuxin Wu, Saining Xie, and Ross Girshick. Momentum contrast for unsupervised visual representation learning. In *Proceedings of the IEEE/CVF Conference on Computer Vision and Pattern Recognition (CVPR)*, pages 9729–9738, 2020. 2, 5
- [12] Yisheng He, Haibin Huang, Haoqiang Fan, Qifeng Chen, and Jian Sun. Ffb6d: A full flow bidirectional fusion network for 6d pose estimation. In *Proceedings of the IEEE/CVF Conference on Computer Vision and Pattern Recognition (CVPR)*, pages 3003–3013, 2021. 1
- [13] Geoffrey Hinton. Distilling the knowledge in a neural network. *arXiv preprint arXiv:1503.02531*, 2015. 2
- [14] Xiaohu Huang, Hao Zhou, Kun Yao, and Kai Han. Froster: Frozen clip is a strong teacher for open-vocabulary action recognition. In *International Conference on Learning Representations (ICLR)*, 2024. 2, 5, 6
- [15] Yuanmin Huang, Mi Zhang, Daizong Ding, Erling Jiang, Zhaoxiang Wang, and Min Yang. Causalpc: Improving the robustness of point cloud classification by causal effect identification. In *Proceedings of the IEEE/CVF Conference on Computer Vision and Pattern Recognition (CVPR)*, pages 19779–19789, 2024. 2, 3
- [16] Andrew Ilyas, Shibani Santurkar, Dimitris Tsipras, Logan Engstrom, Brandon Tran, and Aleksander Madry. Adversarial examples are not bugs, they are features. *Advances in Neural Information Processing Systems (NeurIPS)*, 32, 2019. 1
- [17] HyunJun Jung, Shun-Cheng Wu, Patrick Ruhkamp, Guangyao Zhai, Hannah Schieber, Giulia Rizzoli, Pengyuan Wang, Hongcheng Zhao, Lorenzo Garattoni, Sven Meier, et al. Housecat6d-a large-scale multi-modal category level 6d object perception dataset with household objects in realistic scenarios. In *Proceedings of the IEEE/CVF Conference on Computer Vision and Pattern Recognition (CVPR)*, pages 22498–22508, 2024. 1, 2, 3, 6, 8
- [18] Diederik P Kingma. Adam: A method for stochastic optimization. *arXiv preprint arXiv:1412.6980*, 2014. 6
- [19] Yuelong Li, Yafei Mao, Raja Bala, and Sunil Hadap. Mrcnet: 6-dof pose estimation with multiscale residual correlation. In *Proceedings of the IEEE/CVF Conference on Computer Vision and Pattern Recognition (CVPR)*, 2024. 1
- [20] Haitao Lin, Zichang Liu, Chilam Cheang, Yanwei Fu, Guodong Guo, and Xiangyang Xue. Sar-net: Shape alignment and recovery network for category-level 6d object pose and size estimation. In *Proceedings of the IEEE/CVF Conference on Computer Vision and Pattern Recognition (CVPR)*, pages 6707–6717, 2022. 2
- [21] Jiehong Lin, Zewei Wei, Zhihao Li, Songcen Xu, Kui Jia, and Yuanqing Li. Dualposenet: Category-level 6d object pose and size estimation using dual pose network with refined learning of pose consistency. In *Proceedings of the IEEE/CVF International Conference on Computer Vision (CVPR)*, pages 3560–3569, 2021. 7
- [22] Jiehong Lin, Zewei Wei, Changxing Ding, and Kui Jia. Category-level 6d object pose and size estimation using self-supervised deep prior deformation networks. In *European Conference on Computer Vision (ECCV)*, pages 19–34. Springer, 2022. 1, 6
- [23] Jiehong Lin, Zewei Wei, Yabin Zhang, and Kui Jia. Vi-net: Boosting category-level 6d object pose estimation via learning decoupled rotations on the spherical representations. In *Proceedings of the IEEE/CVF International Conference on Computer Vision (CVPR)*, pages 14001–14011, 2023. 1, 2, 6, 7, 3
- [24] Xiao Lin, Deming Wang, Guangliang Zhou, Chengju Liu, and Qijun Chen. Transpose: 6d object pose estimation with geometry-aware transformer. *Neurocomputing*, 589:127652, 2024. 1
- [25] Xiao Lin, Wenfei Yang, Yuan Gao, and Tianzhu Zhang. Instance-adaptive and geometric-aware keypoint learning for category-level 6d object pose estimation. In *Proceedings of the IEEE/CVF Conference on Computer Vision and Pattern Recognition (CVPR)*, pages 21040–21049, 2024. 1, 2, 3, 5, 6, 7, 8

- [26] Xiao Lin, Minghao Zhu, Ronghao Dang, Guangliang Zhou, Shaolong Shu, Feng Lin, Chengju Liu, and Qijun Chen. Clipose: Category-level object pose estimation with pre-trained vision-language knowledge. *IEEE Transactions on Circuits and Systems for Video Technology (TCSVT)*, 2024. [1](#), [2](#), [5](#), [6](#), [7](#)
- [27] Bing Liu, Dong Wang, Xu Yang, Yong Zhou, Rui Yao, Zhiwen Shao, and Jiaqi Zhao. Show, deconfound and tell: Image captioning with causal inference. In *Proceedings of the IEEE/CVF Conference on Computer Vision and Pattern Recognition (CVPR)*, pages 18041–18050, 2022. [3](#)
- [28] Jianhui Liu, Yukang Chen, Xiaoqing Ye, and Xiaojuan Qi. Ist-net: Prior-free category-level pose estimation with implicit space transformation. In *Proceedings of the IEEE/CVF International Conference on Computer Vision (ICCV)*, pages 13978–13988, 2023. [2](#), [5](#), [7](#)
- [29] Jian Liu, Wei Sun, Chongpei Liu, Hui Yang, Xing Zhang, and Ajmal Mian. Mh6d: Multi-hypothesis consistency learning for category-level 6-d object pose estimation. *IEEE Transactions on Neural Networks and Learning Systems (TNNLS)*, 2024. [1](#), [7](#), [3](#)
- [30] Weiyang Liu, Zhen Liu, Liam Paull, Adrian Weller, and Bernhard Schölkopf. Structural causal 3d reconstruction. In *European Conference on Computer Vision (ECCV)*, pages 140–159. Springer, 2022. [3](#)
- [31] Xingyu Liu, Gu Wang, Yi Li, and Xiangyang Ji. Catre: Iterative point clouds alignment for category-level object pose refinement. In *European Conference on Computer Vision (ECCV)*, pages 499–516. Springer, 2022. [6](#), [7](#), [3](#)
- [32] Yang Liu, Guanbin Li, and Liang Lin. Cross-modal causal relational reasoning for event-level visual question answering. *IEEE Transactions on Pattern Analysis and Machine Intelligence (TPAMI)*, 45(10):11624–11641, 2023. [5](#)
- [33] Xu Ma, Can Qin, Haoxuan You, Haoxi Ran, and Yun Fu. Rethinking network design and local geometry in point cloud: A simple residual mlp framework. In *International Conference on Learning Representations (ICLR)*, 2022. [8](#), [2](#)
- [34] Eric Marchand, Hideaki Uchiyama, and Fabien Spindler. Pose estimation for augmented reality: a hands-on survey. *IEEE Transactions on Visualization and Computer Graphics (TVCG)*, 22(12):2633–2651, 2015. [1](#)
- [35] Maxime Oquab, Timothée Darcet, Théo Moutakanni, Huy Vo, Marc Szafraniec, Vasil Khalidov, Pierre Fernandez, Daniel Haziza, Francisco Massa, Alaaeldin El-Nouby, et al. Dinov2: Learning robust visual features without supervision. *Transactions on Machine Learning Research Journal (TMLR)*, pages 1–31, 2024. [3](#)
- [36] J Pearl. *Causality*. Cambridge university press, 2009. [2](#), [3](#), [4](#)
- [37] Judea Pearl. *Causal inference in statistics: a primer*. John Wiley & Sons, 2016. [2](#), [3](#), [4](#)
- [38] Judea Pearl and Dana Mackenzie. *The book of why: the new science of cause and effect*. Basic books, 2018. [1](#)
- [39] Yun Peng, Xiao Lin, Nachuan Ma, Jiayuan Du, Chuangwei Liu, Chengju Liu, and Qijun Chen. Sam-lad: Segment anything model meets zero-shot logic anomaly detection. *arXiv preprint arXiv:2406.00625*, 2024. [3](#)
- [40] Charles Ruizhongtai Qi, Li Yi, Hao Su, and Leonidas J Guibas. Pointnet++: Deep hierarchical feature learning on point sets in a metric space. In *Advances in Neural Information Processing Systems (NeurIPS)*, 30, 2017. [3](#), [6](#), [8](#), [1](#), [2](#)
- [41] Alec Radford, Jong Wook Kim, Chris Hallacy, Aditya Ramesh, Gabriel Goh, Sandhini Agarwal, Girish Sastry, Amanda Askell, Pamela Mishkin, Jack Clark, et al. Learning transferable visual models from natural language supervision. In *International Conference on Machine Learning (ICML)*, pages 8748–8763. PMLR, 2021. [2](#)
- [42] Leslie N Smith. Cyclical learning rates for training neural networks. In *2017 IEEE winter conference on applications of computer vision (WACV)*, pages 464–472. IEEE, 2017. [6](#)
- [43] Meng Tian, Marcelo H Ang, and Gim Hee Lee. Shape prior deformation for categorical 6d object pose and size estimation. In *European Conference on Computer Vision (ECCV)*, pages 530–546. Springer, 2020. [2](#), [3](#), [7](#)
- [44] Jonathan Tremblay, Thang To, Balakumar Sundaralingam, Yu Xiang, Dieter Fox, and Stan Birchfield. Deep object pose estimation for semantic robotic grasping of household objects. *arXiv preprint arXiv:1809.10790*, 2018. [1](#)
- [45] Shinji Umeyama. Least-squares estimation of transformation parameters between two point patterns. *IEEE Transactions on Pattern Analysis and Machine Intelligence (TPAMI)*, 13(04):376–380, 1991. [2](#)
- [46] Ashish Vaswani, Noam Shazeer, Niki Parmar, Jakob Uszkoreit, Llion Jones, Aidan N Gomez, Łukasz Kaiser, and Illia Polosukhin. Attention is all you need. *Advances in Neural Information Processing Systems (NeurIPS)*, 30, 2017. [5](#)
- [47] Chen Wang, Danfei Xu, Yuke Zhu, Roberto Martín-Martín, Cewu Lu, Li Fei-Fei, and Silvio Savarese. Densefusion: 6d object pose estimation by iterative dense fusion. In *Proceedings of the IEEE/CVF Conference on Computer Vision and Pattern Recognition (CVPR)*, pages 3343–3352, 2019. [1](#)
- [48] He Wang, Srinath Sridhar, Jingwei Huang, Julien Valentin, Shuran Song, and Leonidas J Guibas. Normalized object coordinate space for category-level 6d object pose and size estimation. In *Proceedings of the IEEE/CVF Conference on Computer Vision and Pattern Recognition (CVPR)*, pages 2642–2651, 2019. [2](#), [3](#), [6](#), [7](#), [8](#)
- [49] Liuyi Wang, Zongtao He, Ronghao Dang, Mengjiao Shen, Chengju Liu, and Qijun Chen. Vision-and-language navigation via causal learning. In *Proceedings of the IEEE/CVF Conference on Computer Vision and Pattern Recognition (CVPR)*, pages 13139–13150, 2024. [1](#), [3](#), [4](#), [5](#)
- [50] Pengyuan Wang, HyunJun Jung, Yitong Li, Siyuan Shen, Rahul Parthasarathy Srikant, Lorenzo Garattoni, Sven Meier, Nassir Navab, and Benjamin Busam. Phocal: A multi-modal dataset for category-level object pose estimation with photometrically challenging objects. In *Proceedings of the IEEE/CVF Conference on Computer Vision and Pattern Recognition (CVPR)*, pages 21222–21231, 2022. [2](#)
- [51] Tan Wang, Chang Zhou, Qianru Sun, and Hanwang Zhang. Causal attention for unbiased visual recognition. In *Proceedings of the IEEE/CVF International Conference on Computer Vision (ICCV)*, pages 3091–3100, 2021. [3](#)
- [52] Zhirong Wu, Yuanjun Xiong, Stella X Yu, and Dahua Lin. Unsupervised feature learning via non-parametric instance

- discrimination. In *Proceedings of the IEEE Conference on Computer Vision and Pattern Recognition (CVPR)*, pages 3733–3742, 2018. 5
- [53] Le Xue, Ning Yu, Shu Zhang, Artemis Panagopoulou, Junnan Li, Roberto Martín-Martín, Jiajun Wu, Caiming Xiong, Ran Xu, Juan Carlos Niebles, et al. Ulip-2: Towards scalable multimodal pre-training for 3d understanding. In *Proceedings of the IEEE/CVF Conference on Computer Vision and Pattern Recognition (CVPR)*, pages 27091–27101, 2024. 2, 5, 8, 1, 3
- [54] Xu Yang, Hanwang Zhang, and Jianfei Cai. Deconfounded image captioning: A causal retrospect. *IEEE Transactions on Pattern Analysis and Machine Intelligence (TPAMI)*, 45(11):12996–13010, 2021. 3, 5
- [55] Xu Yang, Hanwang Zhang, Guojun Qi, and Jianfei Cai. Causal attention for vision-language tasks. In *Proceedings of the IEEE/CVF Conference on Computer Vision and Pattern Recognition (CVPR)*, pages 9847–9857, 2021. 3
- [56] Xumin Yu, Lulu Tang, Yongming Rao, Tiejun Huang, Jie Zhou, and Jiwen Lu. Point-bert: Pre-training 3d point cloud transformers with masked point modeling. In *Proceedings of the IEEE/CVF Conference on Computer Vision and Pattern Recognition (CVPR)*, pages 19313–19322, 2022. 6, 8, 1, 2
- [57] Hua Zhang, Liqiang Xiao, Xiaochun Cao, and Hassan Foroosh. Multiple adverse weather conditions adaptation for object detection via causal intervention. *IEEE Transactions on Pattern Analysis and Machine Intelligence (TPAMI)*, 46(3):1742–1756, 2022. 3
- [58] Jiyao Zhang, Mingdong Wu, and Hao Dong. Genpose: generative category-level object pose estimation via diffusion models. In *Proceedings of the 37th International Conference on Neural Information Processing Systems (NeurIPS)*, pages 54627–54644, 2023. 7
- [59] Letian Zhang, Xiaotong Zhai, Zhongkai Zhao, Yongshuo Zong, Xin Wen, and Bingchen Zhao. What if the tv was off? examining counterfactual reasoning abilities of multi-modal language models. In *Proceedings of the IEEE/CVF Conference on Computer Vision and Pattern Recognition (CVPR)*, pages 21853–21862, 2024. 3
- [60] Mengchen Zhang, Tong Wu, Tai Wang, Tengfei Wang, Ziwei Liu, and Dahua Lin. Omni6d: Large-vocabulary 3d object dataset for category-level 6d object pose estimation. *arXiv preprint arXiv:2409.18261*, 2024. 1, 2, 3
- [61] Xiangdong Zhang, Shaofeng Zhang, and Junchi Yan. Pcp-mae: Learning to predict centers for point masked autoencoders. *arXiv preprint arXiv:2408.08753*, 2024. 2
- [62] Linfang Zheng, Chen Wang, Yinghan Sun, Esha Dasgupta, Hua Chen, Ales Leonardis, Wei Zhang, and Hyung Jin Chang. Hs-pose: Hybrid scope feature extraction for category-level object pose estimation. *arXiv preprint arXiv:2303.15743*, 2023. 1, 2, 3, 7
- [63] Linfang Zheng, Tze Ho Elden Tse, Chen Wang, Yinghan Sun, Hua Chen, Ales Leonardis, Wei Zhang, and Hyung Jin Chang. Georef: Geometric alignment across shape variation for category-level object pose refinement. In *Proceedings of the IEEE/CVF Conference on Computer Vision and Pattern Recognition (CVPR)*, pages 10693–10703, 2024. 1, 3, 6, 7
- [64] Guangliang Zhou, Deming Wang, Yi Yan, Huiyi Chen, and Qijun Chen. Semi-supervised 6d object pose estimation without using real annotations. *IEEE Transactions on Circuits and Systems for Video Technology (TCSVT)*, 32(8): 5163–5174, 2021. 1
- [65] Minghao Zhu, Xiao Lin, Ronghao Dang, Chengju Liu, and Qijun Chen. Fine-grained spatiotemporal motion alignment for contrastive video representation learning. In *Proceedings of the 31st ACM International Conference on Multimedia (ACMMM)*, pages 4725–4736, 2023. 5
- [66] Minghao Zhu, Zhengpu Wang, Mengxian Hu, Ronghao Dang, Xiao Lin, Xun Zhou, Chengju Liu, and Qijun Chen. Mote: Reconciling generalization with specialization for visual-language to video knowledge transfer. *arXiv preprint arXiv:2410.10589*, 2024. 2, 5
- [67] Lu Zou, Zhangjin Huang, Naijie Gu, and Guoping Wang. 6d-vit: Category-level 6d object pose estimation via transformer-based instance representation learning. *IEEE Transactions on Image Processing (TIP)*, 31:6907–6921, 2022. 7